THE JOURNAL OF PHYSICAL CHEMISTRY C

Article

pubs.acs.org/JPCC

Adsorption and Activation of CO on Co_3O_4(111) Thin Films

P. Ferstl,[†] S. Mehl,[‡] M. A. Arman,[§] M. Schuler,[†] A. Toghan,[‡,∥] B. Laszlo,[⊥] Y. Lykhach,[‡] O. Brummel,[‡] E. Lundgren,[§] J. Knudsen,[§,#] L. Hammer,[†] M. A. Schneider,*[,†] and J. Libuda*[,‡,○]

[†]Lehrstuhl für Festkörperphysik, Friedrich-Alexander-Universität Erlangen-Nürnberg, Staudtstrasse 7, 91058 Erlangen, Germany

[‡]Lehrstuhl für Physikalische Chemie II and [○]Erlangen Catalysis Resource Center, Friedrich-Alexander-Universität Erlangen-Nürnberg, Egerlandstrasse 3, 91058 Erlangen, Germany

[§]Division of Synchrotron Radiation Research and [#]MAX IV Laboratory, Lund University Box 118, 22100 Lund, Sweden

[∥]Chemistry Department, Faculty of Science, South Valley University, 83523 Qena, Egypt

[⊥]Department of Physical Chemistry and Materials Science, University of Szeged, H-6720 Szeged, Aradi vértanúk tere 1, Hungary

Supporting Information

ABSTRACT: To explore the catalytic properties of cobalt oxide at the atomic level, we have studied the interaction of CO and O_2 with well-ordered Co_3O_4(111) thin films using scanning tunneling microscopy (STM), high-resolution X-ray photoelectron spectroscopy (HR-XPS), infrared reflection absorption spectroscopy (IRAS), and temperature-programmed desorption spectroscopy (TPD) under ultrahigh vacuum (UHV) conditions. At low coverage and temperature, CO binds to surface Co^{2+} ions on the (111) facets. At larger exposure, a compressed phase is formed in which additional CO is located at sites in between the Co^{2+} ions. In addition, a bridging carbonate species forms that is associated with defects such as step edges of Co_3O_4(111) terraces or the side facets of the (111) oriented grains. Preadsorbed oxygen neither affects CO adsorption at low coverage nor the formation of the surface carbonate, but it blocks formation of the high coverage CO phase. Desorption of the molecularly bound CO occurs up to 180 K, whereas the surface carbonate decomposes in a broad temperature range up to 400 K under the release of CO and, to a lesser extent, of CO_2. Upon strong loss of crystalline oxygen, the Co_3O_4 grains eventually switch to the CoO rocksalt structure.

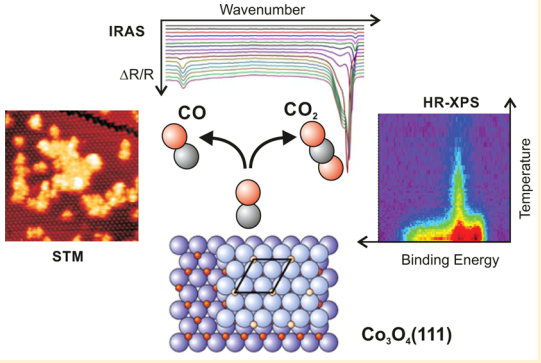

1. INTRODUCTION

Cobalt oxide nanomaterials have recently attracted attention because of their application potential in the fields of heterogeneous catalysis,[1−4] energy-related materials,[5] catalysis,[6−8] and electrocatalysis.[9−11] Among the specific applications are, for example, the production of hydrogen by reforming of hydrocarbon oxygenates such as ethanol,[7,8,12] the low temperature CO oxidation,[1,3,13−20] and the selective oxidation of CO (PROX, for removal of CO from the hydrogen feed of fuel cells),[6] the oxidation of methane and volatile organic compounds (VOC),[2,21−27] and both the oxygen reduction reaction (ORR) and the oxygen evolution reaction (OER) in electrocatalysis.[9,10,28] It is noteworthy that in these applications cobalt oxide often replaces noble metals, such as platinum. With an abundance in the earth crust that is about 5000× higher than that of platinum, this holds the potential of providing low-cost alternatives to noble metal catalysts in the above-mentioned processes.

In various respects the catalytic behavior of cobalt oxide is, however, very different from its noble metal counterparts. One of the unique features is the outstanding structure dependency of the activity of nanostructured cobalt oxide.[4] For example, it has been recognized early that the spinel-type Co_3O_4 shows high activity for the low-temperature CO oxidation, in contrast to the rocksalt-type CoO.[13] Further, Haruta and co-workers demonstrated recently very high activity of Co_3O_4 nanorods for CO oxidation at temperatures as low as 196 K.[1] These nanorods exposed a large fraction of (110) facets. Different reaction pathways have been proposed that could be responsible for the catalytic activity. Among these pathways are (i) the reaction of CO, adsorbed at a Co^{3+} center, with a down coordinated lattice oxygen,[1] (ii) the activation of molecular oxygen at 2-fold coordinated oxygen vacancy sites, followed by reaction with a coadsorbed CO,[17] and (iii) the reaction of CO with 2-fold coordinated lattice oxygen, followed by vacancy diffusion and oxygen dissociation at double vacancies.[29] Quite naturally, even less is known on the microscopic reaction mechanisms for more complex reactions such as those that involve larger hydrocarbons and hydrocarbon oxygenates. Different active sites and structural features have

Received: April 30, 2015
Revised: June 24, 2015
Published: June 30, 2015

DOI: 10.1021/acs.jpcc.5b04145
J. Phys. Chem. C 2015, 119, 16688−16699

been suggested to play a role.[4] For example, Co_3O_4 nanosheets with predominately (112) facets were shown to be particularly active for CH_4 oxidation.[30,31] Here, oxygen activation in the presence of oxygen vacancies and surface Co^{2+} ions were related to the high activity for methane activation and VOC oxidation.

In the above-mentioned catalytic studies on nanomaterials there are two principal problems that complicate the interpretation of structure−reactivity correlations. First, the atomic structure of the nanomaterial facets under reaction conditions is generally unknown, even if their shape is well-controlled. In fact, for complex oxides of a given surface orientation, a variety of bulk terminations are conceivable. Therefore, apart from the complications arising from possible surface reconstructions, the choice of a specific bulk termination (to facilitate comparison with theoretical calculations) may produce misleading results. Second, coadsorbates may be present at the surface, in particular, at low reaction temperatures. These coadsorbates may modify the adsorption energetics and the reaction pathways.

In the present work we follow a model catalysis approach to the cobalt oxide surface chemistry.[32,33] We aim to study structure−reactivity relations on atomically defined cobalt oxide surfaces under well-controlled conditions in ultrahigh vacuum (UHV). We take advantage of the fact that a variety of well-ordered Co_3O_4 and CoO films can be grown on Ir(100).[34−38] In a unique fashion, these films allow to vary the stoichiometry, the surface orientation, the film thickness, and the defect density. Over the last years, many of these structures have been characterized in great detail using low energy electron diffraction (LEED) $I-V$ analysis and scanning tunneling microscopy (STM). In the present work, we start from a well-ordered and well-characterized $Co_3O_4(111)$ film[34,35] and explore its interaction with CO and O_2. We identify the adsorption sites, interaction mechanisms, and possible activation mechanisms for oxidation of CO. The present work will serve as a starting point for future studies that aim at the controlled modification of the $Co_3O_4(111)$ surface to design atomically controlled sites for CO, hydrocarbon, and oxygen activation.

2. EXPERIMENTAL SECTION

The experiments were performed in three different UHV systems. IRAS, TPD, and STM measurements were performed in two separate laboratories at the Universität Erlangen-Nürnberg, Germany, and HR-XPS was performed at the beamline I311 at the MAX IV Laboratory (Lund, Sweden).

IRAS Experiments. The IRAS experiments were performed in a UHV system with a base pressure of $p = 2 \times 10^{-10}$ mbar, containing standard preparation characterization methods (low energy electron diffraction, Auger electron spectroscopy, temperature-programmed desorption). The infrared (IR) measurements were performed with a vacuum Fourier-Transform infrared spectrometer (Bruker VERTEX 80v) equipped with a liquid-nitrogen cooled narrow-band mercury cadmium telluride detector. The spectrometer is coupled via differentially pumped KBr windows to the UHV system. The present measurements were performed in a remote-controlled mode (National Instruments (NI) and LabView (NI) interface) by dosing pulses of CO via a gas doser equipped with an electromagnetic valve and subsequent acquisition of the IR spectra. The low pressure reservoir of the doser was filled with CO (Messer, 4.7) that was further purified using a liquid nitrogen cold trap to remove possible traces of volatile carbonyls. Before the experiment, a background spectrum was taken (200 scans, sampling rate 10 kHz, resolution 4 cm^{-1}, 110 s). For each experiment, 15 pulses of CO corresponding to exponentially increasing gas doses were admitted. After each CO pulse, a spectrum was taken (200 scans, sampling rate 10 kHz, resolution 4 cm^{-1}, 110 s).

STM and TPD Experiments. STM and TPD experiments were conducted in a second UHV chamber at a base pressure of 2×10^{-11} mbar. Sample preparation, LEED, TPD, and STM were performed in situ. LEED and TPD were performed on a liquid-nitrogen-cooled manipulator. The TPD spectra were taken with a quadrupole mass spectrometer (QMS) equipped with Feulner cup,[39] the entrance of the nozzle was placed ∼0.5 mm in front of the sample surface, and only gases desorbing from the area of the Ir crystal could enter the QMS. To calibrate the amount of CO desorbed from the sample, the desorption of CO from the well-known Ir(100)-c(2 × 2)-CO structure[40] was measured using exactly the same geometry. Due to the small heating power needed at temperatures below 100 K, the employed temperature ramp was nonlinear. The TPD spectra shown are plotted against time and the axis was relabeled using the temperature at the given instance. For STM experiments (at 300 K), the sample was transferred to a separate part of the UHV chamber and electrochemically etched tungsten tips were used.

HR-XPS Experiments. The HR-XPS experiments were conducted at the high resolution X-ray photoemission spectroscopy endstation at beamline I311[41] at the MAX IV Laboratory. All spectra are collected in normal emission with photon energies of 380 eV (C 1s) and 625 eV (O 1s), respectively. During measurements, the sample was moved across the X-ray beam at a speed of 5 μm/s. This velocity ensured that spectra taken were not affected by beam-induced desorption or reactions as judged from the time independence of spectra at constant temperature. For the curve fitting, we used symmetric Voigt components after subtracting a polynomial background.

Sample Preparation. The preparation of the $Co_3O_4(111)$ films on Ir(100) was previously described in the literature.[34,35] We employed here a slightly modified procedure that could be carried out in all used UHV systems with utmost control of the relevant process parameters like substrate cleanliness and structure, Co amount, temperature, and O_2 partial pressure. In all setups, the sample was mounted according to the respective needs of the experiment such that heating to 1500 K and cooling to 100 K or below with liquid nitrogen could be achieved. First, the Ir(100) crystal was cleaned by several cycles of ion bombardment (2 keV, 10 μA) for 60 min with Ar (Linde 6.0, Air Liquide 4.8) followed by annealing for 3 min to 1273 K. This procedure was repeated until the crystal showed a high-quality Ir(100)-(5 × 1) reconstruction as judged by LEED at room temperature or below. Subsequently, the (5 × 1) reconstruction was lifted by producing the Ir(100)-(2 × 1)-O structure by cooling down the sample from 1200 K to room temperature in 10^{-8} mbar oxygen (Linde 5.0, AGA 5.0). The eventual preparation of the Co_3O_4 film involved the use of a O_2 gas doser aiming at the surface at the same time as the Co source, a commercial electron-beam evaporator (Focus EFM3, 2 mm Co rod, Alfa Aesar 99,995%, Good fellow 99.99%). This allowed the local oxygen pressure at the surface to be well above 5×10^{-6} mbar during growth. The evaporation rate of the Co source was calibrated using a quartz microbalance and

DOI: 10.1021/acs.jpcc.5b04145
J. Phys. Chem. C 2015, 119, 16688−16699

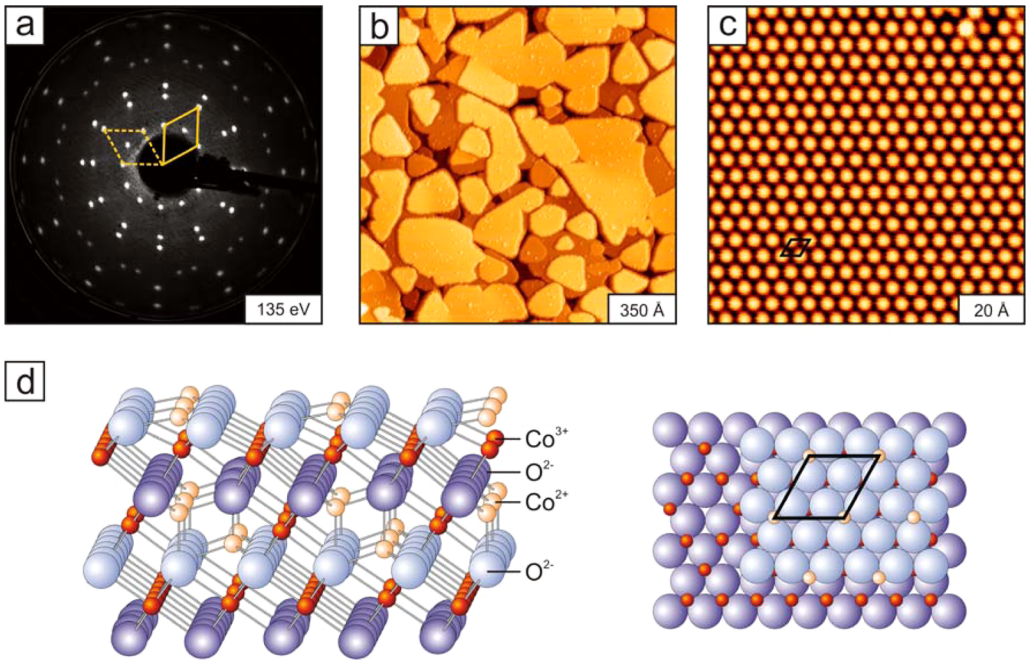

Figure 1. (a) LEED pattern showing the $Co_3O_4(111)$ film on Ir(100); (b) large-scale STM image showing the morphology of the as-prepared $Co_3O_4(111)$ film; (c) atomically resolved STM image of a single terrace on the $Co_3O_4(111)$ film; (d) structural model of the $Co_3O_4(111)$ film on Ir(100) (see text for details).

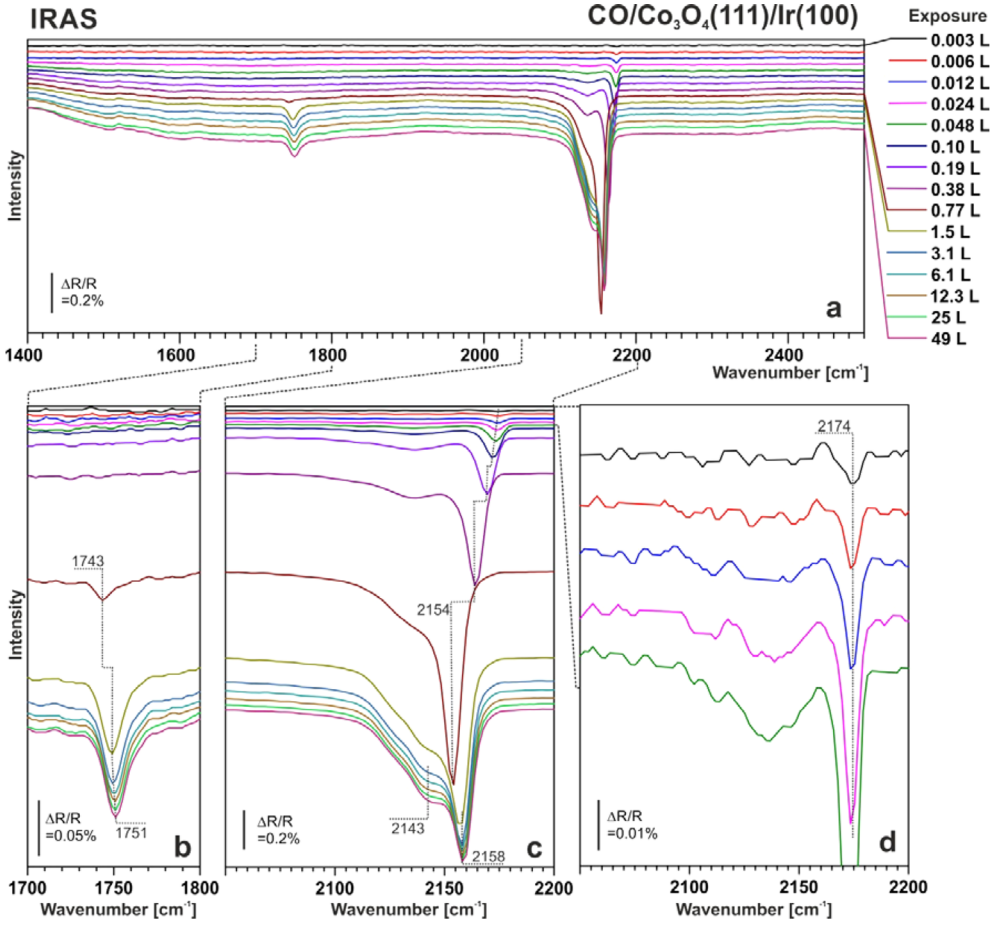

Figure 2. (a) IRAS taken after exposure of $Co_3O_4(111)$/Ir(100) to different doses of CO at 100 K; (b, c) zoom into selected spectral regions; (d) CO stretching frequency region in the limit of very low CO exposures.

DOI: 10.1021/acs.jpcc.5b04145
J. Phys. Chem. C 2015, 119, 16688−16699

by producing other two-dimensional cobalt oxide structures that require exact amounts of Co expressed in monolayer equivalents (MLEs).[36] One MLE corresponds to a full monolayer coverage of the Ir(100) surface. For obtaining the $Co_3O_4(111)$ films, 15 MLE of Co were evaporated under steady oxygen flow with a rate of 1 ML/min at 300 K sample temperature. Subsequently, the roughly 5 nm thick films were annealed keeping the same oxygen flux for 2 min at 523 K and finally briefly heated in UHV to 673 K to improve the degree of ordering.

3. RESULTS AND DISCUSSION

3.1. Structure and Defects of $Co_3O_4(111)$/Ir(100) Films. Figure 1 shows a summary of structural features of the films that are most relevant for the following discussion. LEED images (Figure 1a) taken at 80 K after the preparation of the $Co_3O_4(111)$ films reveal a high degree of structural homogeneity and long-range order without contributions of the underlying Ir(100) substrate. From the previous structural analysis[34] it is known that the surface of the spinel $Co_3O_4(111)$ films is terminated by Co atoms that would nominally correspond to the Co^{2+} ions of the bulk crystal (see structure model in Figure 1d). The distance between Co atoms in the surface layer is 5.72 Å, identical to the corresponding distance in the bulk crystal. The surface unit cell (indicated in the LEED pattern in Figure 1a and in the structure model in Figure 1d has an area of 28.3 $Å^2$. One of the base vectors of the hexagonal Co_3O_4 cell is aligned along [011] of the Ir substrate and the film grows in twins of two orthogonal domains on Ir(100). Large scale STM images like the one shown in Figure 1b reveal that the film consists of large grains with a diameter of up to 500−1000 Å interspersed with some smaller ones. There are steps between (111) terraces of the same grain with a step height of mainly 4.7 Å (single repeat unit). The latter value corresponds to a single repetition unit of the spinel structure. Figure 1c shows an atomically resolved STM topography. We interpret this image to represent the Co lattice at the surface. From many such images, we conclude that the grains exhibit almost perfect surfaces with total point defect density of less than one percent of the Co sites on the (111) terraces. Most of the point defects are adsorbates or missing Co atoms. We infer from the STM images that the thickness variation of the grains is 2−3 repeat units and from the missing beams of the Ir substrate in the LEED image we conclude that the Ir surface is completely covered by Co_3O_4 even between the grains. However, due to the geometry of the STM tip the depth and structure of the grain boundaries cannot be determined with certainty. As a consequence the surface area at the steps and side facets of the Co_3O_4 grains may be up to 20% of the surface area of the top faces and the side facets may be rich in defect sites.

3.2. Adsorption of CO with and without Preadsorption of Oxygen at 100 K. We have probed the interaction of CO with the pristine $Co_3O_4(111)$ film using IRAS, HR-XPS, and TPD. The IRAS spectra taken during CO exposure at a substrate temperature of 100 K are displayed in Figure 2. A remote-controlled doser device was used to obtain reproducible CO exposures over a large range (see Experimental Section). After taking the reference spectrum, the sample was exposed to a preprogrammed series of exponentially increasing doses of CO and IR spectra were automatically acquired after each dose. Thus, an exposure range of more than 4 orders of magnitude could be covered, ranging from 0.003 to 49 L (1 L (Langmuir) = 1×10^{-6} Torr·s).

Overview spectra are shown in Figure 2a. The main bands appear in the spectral region between 2100 and 2200 cm^{-1}. In addition, a weak band appears at around 1750 cm^{-1} at CO doses exceeding 1 L (Figure 2b). Figure 2c shows the development of the main bands over the full coverage range. The spectra in the limit of very low coverage are scaled up in Figure 2d. It is noteworthy that the excellent signal/noise ratio which could be reached with the present experimental setup allows us to identify adsorbed CO down to coverages of about 0.1% of a monolayer (ML). At a CO exposure of 0.003 L we observe a band at 2174 cm^{-1} ($\Delta R/R \sim 0.005\%$), which undergoes a redshift to 2154 cm^{-1} with increasing coverage. The main peak is accompanied by a weak shoulder at 2140 cm^{-1}. At exposures exceeding 1 L, this shoulder (2143 cm^{-1}) drastically increases in intensity, while the main peak undergoes a slight blue shift to 2158 cm^{-1}. At exposures exceeding 3 L, no further change in the spectra is observed. Interestingly, formation of the shoulder at 2143 cm^{-1} is accompanied by the appearance of a weak peak at 1743 cm^{-1}, which grows in intensity and undergoes a slight blue shift to 1751 cm^{-1} up to exposures of 3 L. Similarly, as observed for the main peak, this feature also does not change at exposures exceeding 3 L.

The bands around 2150 cm^{-1} can be attributed to weakly adsorbed molecular CO species on the Co_3O_4 surface. Surprisingly, rather few studies are available in the literature that provide high quality IR spectra of weakly adsorbed CO on ordered oxide surfaces. The best studied systems are CO/MgO(100)[42−45] and $CO/Fe_3O_4(111)/Pt(111)$,[46] with the latter oxide film being closely related to $Co_3O_4(111)$/Ir(100) from the structural point of view.

CO adsorption on MgO(100) was initially investigated by Heidberg and co-workers[42] using vacuum-cleaved single crystal surfaces and later on studied on well-shaped nanoparticles by Zecchina and co-workers.[43−45] On MgO(100) CO adsorbs in a perpendicular geometry at Mg^{2+} sites up to coverages of $\theta < 0.25$.[42] With increasing coverage, the CO stretching band shows a red shift of 9 cm^{-1} from 2157 to 2148 cm^{-1}, arising from a combination of static and dynamic coupling effects.[45] The evolution of the spectral shape of the CO bands on MgO(100) is similar to our spectra on $Co_3O_4(111)$. We observe, however, a higher CO frequency in the low coverage limit and a larger coverage dependent red-shift (Δ = 20 cm^{-1}, from 2174 to 2154 cm^{-1}) than on MgO. Interestingly, the CO density on MgO(100) at $\theta = 0.25$ is 2.8×10^{14} cm^{-2}.[43] This value is about 20% smaller than the density of surface Co^{2+} ions in $Co_3O_4(111)$, which amounts to 3.5×10^{14} cm^{-2}.[35] Based on this comparison, we suggest that in the low coverage regime (0−0.77 L) CO is adsorbed at the surface Co^{2+} sites. The stronger blue shift of the CO stretching band in comparison to MgO(100) can in part be rationalized in terms of a different Stark shift.[43] The Stark shift leads to a blue shift that depends on the strength of the local electric field at the cation site. On $Co_3O_4(111)$, the Co^{2+} ions are positioned 0.32 Å above the O^{2-} ions,[34] in contrast to the MgO(100) surface where cations and anions are coplanar. The situation is to some extent comparable to the more exposed Mg^{2+} ions at nanoparticle edges and corners, which also give rise to stronger blue-shifted bands appearing at 2170 and 2203 cm^{-1}.[43,44] The larger coverage dependence is associated with a stronger dipole

DOI: 10.1021/acs.jpcc.5b04145
J. Phys. Chem. C 2015, 119, 16688−16699

coupling which besides other effects arises from the higher CO density on $Co_3O_4(111)$.

The above assignment is consistent with the work of Lemire et al. who studied CO adsorption on $Fe_3O_4(111)/Pt(111)$.[46] Interestingly, the $Fe_3O_4(111)$ film shows a surface structure and unit cell that is very similar to the $Co_3O_4(111)$. In contrast to Co_3O_4, however, Fe_3O_4 has inverse spinel structure, that is, Fe^{3+} occupy both octahedral and tetrahedral sites. Lemire et al. identified three adsorption sites on $Fe_3O_4(111)$ giving rise to IR bands at 2214−2210, 2154, and 2098−2080 cm^{-1} (low CO coverage−high coverage). On the basis of the rather low vibrational frequency, the authors assigned the principle peak at 2098 cm^{-1} to CO at Fe^{2+} sites and concluded that the $Fe_3O_4(111)$ film is terminated by Fe^{2+} ions and not by Fe^{3+} ions as the bulk structure would suggest. Further, the weaker high frequency band at 2214−2210 cm^{-1} was assigned to CO at Fe^{3+} ions located at structural defect sites. In our case, the principal band at 2174−2154 cm^{-1} is in between the bands assigned to Fe^{2+} and Fe^{3+} and close to CO adsorbed on Mg^{2+}. Our assignment of the principal band at 2174−2154 cm^{-1} to CO adsorbed at Co^{2+} sites appears reasonable, as it agrees with a bulk termination of the film and is consistent with previous structural analysis.[34]

At larger exposure, the CO adsorption behavior on $Co_3O_4(111)$ is rather different from that on $Fe_3O_4(111)$.[46] On the latter surface, only weak bands were observed in addition to the band at 2098−2080 cm^{-1}. These were assigned to CO adsorption at Fe^{3+} defect sites (2210 cm^{-1}) and weak adsorption on the terraces (2154 cm^{-1}). In contrast, the coverage dependence of the spectra on MgO is quite similar to that observed on $Co_3O_4(111)$.[43−45] At higher coverage ($\theta > 0.25$), the peak around 2150 cm^{-1} broadens and develops additional features at lower frequency. These changes are associated with a new adsorbate structure on MgO(100) in which energetically inequivalent sites are occupied. In addition, the CO adopts a slightly tilted orientation. Similar spectral changes are observed on Co_3O_4 at exposures exceeding 0.77 L. Therefore, we suggest the formation of a high coverage phase in which weakly adsorbed CO is adsorbed in between the Co^{2+} sites. The local adsorption site cannot be clearly determined from the present data. One possibility would be a surface dicarbonyl.[47,48] Such a species should, however, be characterized by a symmetric and an asymmetric mode with very different intensities in IRAS. A second possibility would be the occupation of interstitial sites in between the surface Co ions, that is, at sites above the Co^{3+} centers located below the topmost oxygen layer.[34] It should be pointed out that the situation is complicated by the fact that the surface electronic structure of the $Co_3O_4(111)$ film is not entirely clear. Assuming bulk termination and the structure model from the LEED structure analysis,[34] a polar surface is created, and the electrostatic stabilization mechanism has not been established yet.

Finally, we consider the origin of the band around 1750 cm^{-1}. This band has no counterpart, neither on MgO(100) nor on $Fe_3O_4(111)$. Its low intensity suggests that it is not related to a species formed on the regular $Co_3O_4(111)$ facets. We rather associate it with a defect site of the film. The vibrational frequency is within the region of surface carbonates, however, it is close to its upper frequency limit.[49,50] To the best knowledge of the authors carbonate bands above 1700 cm^{-1} have not been reported on cobalt oxide so far. However, bands in this region have been identified on other oxides. On MgO powders bands above 1700 cm^{-1} have been assigned to bidentate carbonates.[50] Recently, Vayssilov et al. performed an extensive theoretical and experimental investigation of surface carbonates on CeO_2.[49] The authors also assigned the highest frequency features between 1720 and 1730 cm^{-1} to the formation of surface bidentates. Note that the formation of weakly bound surface carbonates upon CO exposure at low temperature has previously been observed on other oxide surfaces as well.[51] Based on these considerations, we attribute the feature at 1750 cm^{-1} to a weakly bound bidentate carbonate which is formed at a defect site. A possible type of defect identified in the structural characterization (see section 3.1) are the side facets of the grains and steps between $Co_3O_4(111)$ terraces. The weakly bound carbonate could be formed by binding of CO to two oxygen centers at such step edges.

In the next step we explore the influence of coadsorbed O_2 on the adsorption of CO. In Figure 3 we show the IRAS spectra

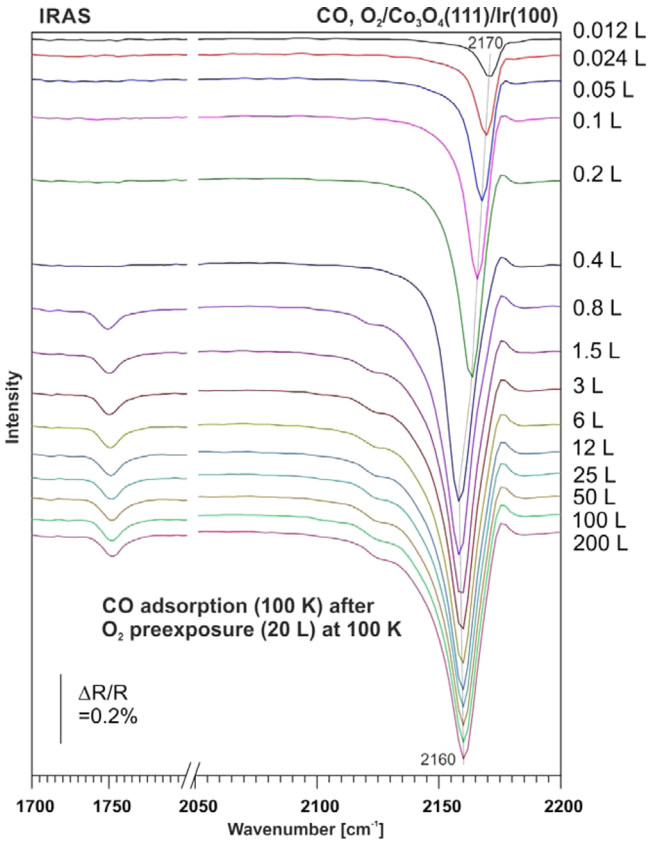

Figure 3. IRAS taken after pre-exposure of $Co_3O_4(111)/Ir(100)$ to 20 L of O_2 at 100 K and subsequent exposure to different doses of CO at 100 K.

obtained after exposure of the $Co_3O_4(111)$ film to 20 L of O_2 at 100 K, followed by successive dosing of CO at 100 K. Apart from the O_2 pre-exposure, the experimental procedure was similar to the one used for adsorption of CO only (see Figure 2). In the limit of small exposure, we observe the appearance of a band at 2171 cm^{-1}, which increases in intensity with increasing CO exposure and undergoes a red-shift to 2160 cm^{-1}. At exposures exceeding 1 L, the band develops a weak shoulder around 2130 cm^{-1}, but the formation of the strong high coverage band at 2140 cm^{-1}, assigned to the compressed CO layer formed on the oxygen-free surface, is completely suppressed. Interestingly, the weak carbonate band

DOI: 10.1021/acs.jpcc.5b04145
J. Phys. Chem. C 2015, 119, 16688−16699

at 1750 cm^{-1} is not influenced by O_2 pre-exposure. Both frequency and intensity are practically identical to the oxygen-free surface.

The different effect of preadsorbed oxygen on the three bands at 2170, 2140, and 1750 cm^{-1} supports the interpretation that the related species are located at different sites, i.e. at Co^{2+} sites on terraces (2170 cm^{-1}), at interstitial sites on terraces (2140 cm^{-1}) and at defects (1750 cm^{-1}) (side facets and steps) of the Co_3O_4 grains. Based on the above observations we suggest that the preadsorbed oxygen blocks CO adsorption at the weakly binding interstitial sites in between the surface Co^{2+} ions. CO adsorption at the more strongly binding Co^{2+} sites is not affected by preadsorbed oxygen. Also, the preadsorbed oxygen has no effect on the carbonate formation at the terrace edges. This observation is in line with the expectation that the interaction of molecular oxygen with the oxygen ions at the terrace edges should be rather weak.

3.3. Monitoring the Thermal Evolution and Desorption of CO by TPD and HR-XPS. To further identify the nature of the adsorbed CO, we have performed HR-XPS after adsorption of CO and during subsequent heating of the sample. Figure 4a shows the C 1s spectrum after exposure to 10 L CO at 85 K.

The experimental spectrum can be fitted with three different components located at binding energies (BEs) of 287.0 (red), 288.5 (blue), and 290.9 eV (green) and having relative intensities of 20, 17, and 63%, respectively (see Figure 4a). The full width at half-maximum (fwhm) of the two components with lowest binding energy are all ~1 eV in contrast to the component at 290.6 eV that is very broad, with a fwhm of 4.6 eV.

To help with the assignment of the different C 1s components we performed temperature-programmed XPS experiments to study their temperature evolution. After dosing 10 L CO at 85 K, we recorded the C 1s energy region while the sample was heated from 85 to 500 K at a heating rate of 20 K/min and while the sample was scanned at a speed of 5 μm/s through the X-ray beam. An image plot showing the evolution of the C 1s region is shown in Figure 4b, while the intensities of the three components (all normalized to 1 at 96 K) are plotted in Figure 4c.

We observe that the intensities of the components at 287.0 eV and at 290.9 eV decrease nearly simultaneously and both components are fully removed at 230 K. In the IRAS data discussed above two different CO adsorption sites were identified: (i) weakly adsorbed CO above surface Co^{2+} ions at small exposures and (ii) even more weakly adsorbed CO above interstitial sites at larger exposures. Concerning the origin of the two features 287.0 and 290.9 eV, one could be tempted to associate these to the two CO species identified in IRAS. However, neither the difference in binding energy nor the different energetic widths of the XPS signature support such an interpretation for a weakly adsorbed CO. The fact that the two features disappear in parallel when the temperature is increased rather suggests that they both originate from the same species. Therefore, we tentatively assign the peaks at 287.0 and 290.9 eV to the main photoemission line and a giant shakeup transition, respectively, originating from weakly bound CO. The binding energy difference between the shakeup transition and the main line (3.9 eV) fits well to what previously has been observed for CO adsorbed on Ni(110), 2.1 eV, Cu(100), 2.5 eV, and Ag(110), 4.2 eV; the shakeup feature may become dominant in weakly bound systems.[52−56]

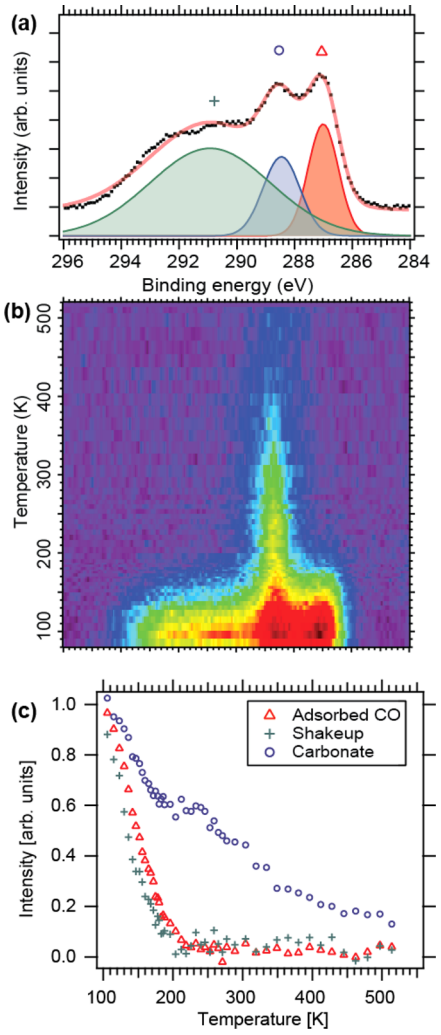

Figure 4. (a) C 1s spectrum after dosing 10 L CO at 85 K onto $Co_3O_4(111)/Ir(100)$. The experimental spectrum is shown with black dots, the fit as a solid line, and the filled curves represent the components of the fit. (b) Image plot of the evolution of the C 1s spectrum as a function of temperature after removal of a polynomial background. (c) Temperature evolution of the intensity of the different components shown in (a) obtained from simultaneous curve fitting the data shown in (b).

In contrast to the components at 287.0 and 290.9 eV that are fully desorbed at 230 K, the component at 288.5 eV decays over a very broad temperature range and remains present on the surface up to 400 K. Based on the higher thermal stability, we associate this feature with the surface carbonate species previously identified in IRAS. The binding energy of 288.5 eV is consistent with those observed for surface carbonates previously, for example on cerium oxide[51] and on oxidized Ag surfaces 287.7−289 eV.[57] Also, the broad temperature range for carbonate decomposition is not unusual for these species on oxides.[49,57]

In the bottom part of Figure 5a we compare the O 1s spectra before (violet) and after (red) dosing of 16 L of CO at 90 K. Before CO dosing, the main peak was located at 529.30 eV and a small shoulder peak component at 528.55 eV. Upon CO dosing they both shift by +0.20 eV, and we assign this effect to an electrostatic shift, which is often observed for adsorption on thin metal oxide films.[58] If we shift the spectrum accordingly (see top part of Figure 5a), it becomes clear that the shape of

DOI: 10.1021/acs.jpcc.5b04145
J. Phys. Chem. C 2015, 119, 16688−16699

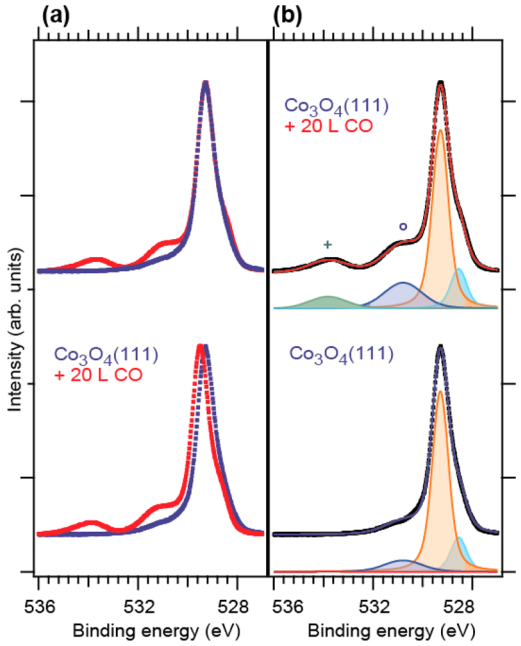

Figure 5. (a) O 1s of $Co_3O_4(111)$ before (blue) and after (red) adsorption of 20 L of CO at 90 K. Spectra calibrated to the Ir bulk peak are shown in the bottom part. The top part the blue spectrum is shifted −0.20 eV otherwise it is identical to the bottom part. (b) Curve fitting of the O 1s region of $Co_3O_4(111)$ before (bottom) and after (top) adsorption of CO.

the main peak remains practically unchanged, while the relative intensity of the shoulder component increases from 0.19 before CO dosing to 0.22 after CO dosing.

In addition to the main peak originating from the $Co_3O_4(111)$ film itself, we observe two new components upon CO dosing shifted by +1.5 and +4.5 eV with respect to the main line (see Figure 5b). To help with the assignment of these two components the O 1s region was followed in situ while heating the sample to 540 K. Figure 6 displays the TP-XPS data from this experiment, and it is evident that the component shifted by +4.5 eV from the main line disappears in the temperature interval between 90 and 250 K. In the same temperature interval, the binding energy of the Co_3O_4 (111) main peak shifts from 529.5 to 529.35 eV. Since the C 1s components at 287.0 and 290.9 eV assigned to weakly adsorbed CO disappear in the same temperature interval we conclude that the O 1s component shifted by +4.5 eV can also be assigned to the weakly adsorbed CO. Further, we note that the disappearance of the shift of the main O 1s peak correlates nicely with the disappearance of the weakly adsorbed CO (see Figure 6c), suggesting that it is mainly this species which is responsible for the shift.

The remaining O 1s component with a BE shift of +1.5 eV should then contain the contribution from the carbonate species observed in the C 1s and IR spectra. Its temperature dependence is, however, relatively complex. The reason is a minority reaction channel to CO_2 that leads to the formation of oxygen vacancies. This will be discussed in section 3.4.

To obtain further insight into the energetics of CO desorption, we have performed TPD experiments as a function of CO exposure. Selected spectra are displayed in Figure 7. Two main features are identified in the temperature region below 300 K. At low exposure a more strongly bound state is populated which gives rise to a desorption maximum close to

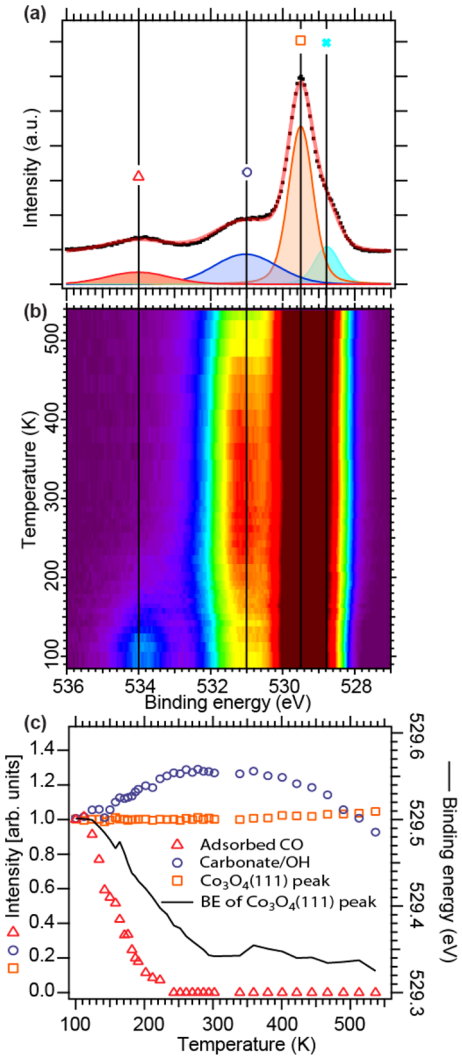

Figure 6. (a) Initial O 1s spectrum after dosing 16 L of CO at 90 K acquired before the heating cycle was started. (b) Image plot showing the development of the O 1s region while heating from 90 to 540 K. (c) Temperature evolution of the intensity of the different components (left *y* axis) shown in (a) obtained from simultaneous curve fitting the data shown in (b). The right *y* axis shows the binding energy of the $Co_3O_4(111)$ main line as a function of temperature.

180 K. With increasing exposure, this feature shifts to lower temperatures. Finally at saturation coverage (top curve in Figure 7), it develops into a shoulder (around 150 K) of a second desorption feature that appears close to 100 K. The low-temperature desorption peak increases with CO exposure. It should be noted, however, that desorption already starts at the lowest adsorption temperatures that could be reached, which implies that the low-temperature state cannot be fully saturated. We note also that, at a temperature above 200 K, a broad and weak CO desorption feature may be discerned that extends up to temperatures around 400 K.

On the basis of the IRAS and the HR-XPS data, we associate the peak between 150 and 180 K with the more strongly adsorbed CO at the Co^{2+} sites, whereas the low temperature desorption peak between 90 and 110 K is caused by the additional CO adsorbed in the compressed adsorbate structure formed at larger exposure. From a simple Redhead analysis, assuming a constant heating rate of 15 $K \cdot s^{-1}$, first order desorption, and a pre-exponential factor of 10^{13} s^{-1}, this value

DOI: 10.1021/acs.jpcc.5b04145
J. Phys. Chem. C 2015, 119, 16688−16699

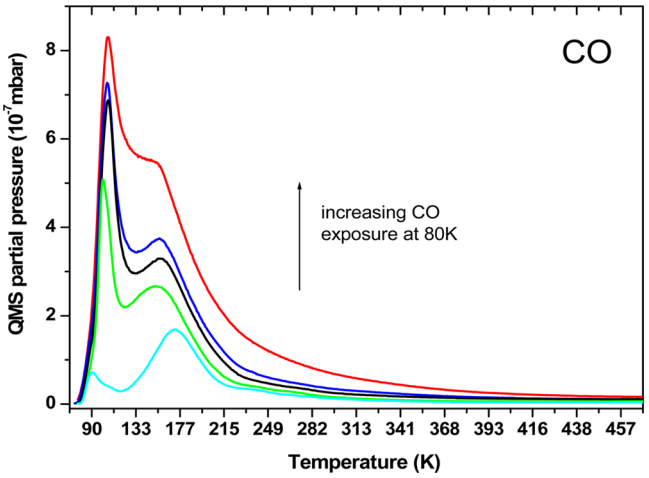

Figure 7. TPD spectra of CO (m/e = 28) on Co_3O_4(111)/Ir(100) recorded as a function of CO coverage after CO adsorbed at 80 K.

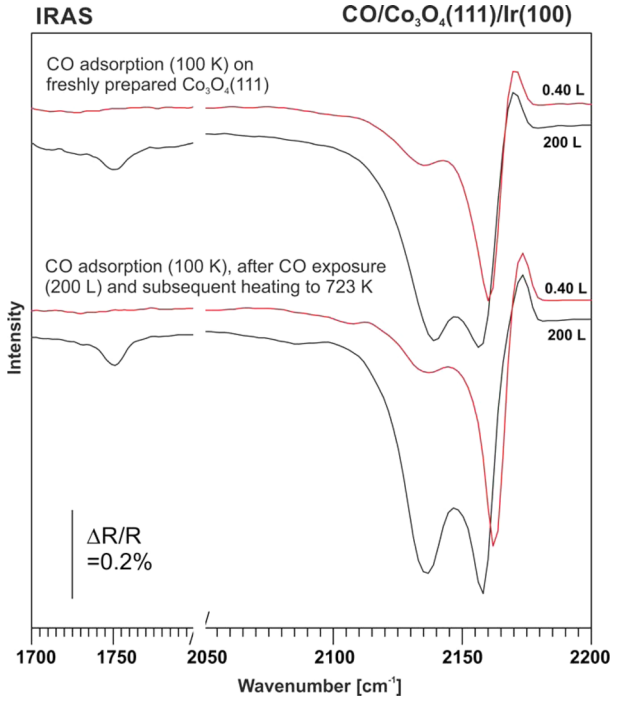

Figure 8. Comparison of IRAS spectra of CO on Co_3O_4(111)/Ir(100) in the low coverage regime (0.4 L) and in the high coverage regime (200 L) at 100 K; (top) pristine Co_3O_4(111)/Ir(100) after preparation; (bottom) after CO exposure (200 L at 100 K) and subsequent annealing to 723 K.

corresponds to desorption activation energies of 36−43 kJ·mol^{-1} for the more strongly bound CO and to an upper limit of 21−26 kJ·mol^{-1} for the weakly bound species (for which desorption starts already at 90 K). We note that the total amount of CO desorbing from the fully saturated Co_3O_4 surface is about twice as high as that from the Ir(100)-c(2 × 1)CO structure that was used for comparison.[40] This would roughly correspond to four CO molecules per Co_3O_4(111) unit cell if the film were perfectly flat and single crystalline. The observation is in agreement with the formation of a compressed structure with more than one CO molecule stabilized per surface unit cell. However, the true CO density is certainly lower than four molecules per regular unit cell due to adsorption at the side facets of the Co_3O_4(111) grains. The broad desorption intensity extending up to higher temperature may at least in part be associated with the surface carbonate formed at irregular sites of the oxide film.

3.4. Reactivity. Next we turn to the reactivity of the Co_3O_4 model surface toward CO. We have explored the reactivity by repeated CO adsorption (100 K) and annealing experiments. A comparison of the IR spectra before and after annealing is displayed in Figure 8 and HR-XPS of the O 1s region before and after repeated annealing is shown in Figure 9. Corresponding TPD and STM data is displayed in Figure 10.

Comparison of the IR spectra of adsorbed CO (see Figure 8) reveals that only minor changes occur upon a single CO adsorption and annealing cycle. All three characteristic CO-induced bands reappear in the second CO experiment with small changes in the band shapes only (the small positive contribution in the IR signals is due to traces of CO adsorbing from the background gas during cooling and before acquisition of the reference spectrum). This observation shows that the majority of CO desorbs molecularly without reacting with the oxide lattice. The TPD spectra (Figure 10a) confirm this conclusion, but also indicate a small fraction of CO oxidation, as a weak and broad CO_2 desorption feature is observed between 200 and 400 K. Note that in this temperature regime the surface carbonate is the only CO-derived species that persists on the surface. We may conclude that the majority of the surface carbonate desorbs as CO, but a small fraction is also converted to CO_2.

We also investigated the changes in the O 1s region upon repeated CO adsorption and annealing cycles by HR-XPS. In

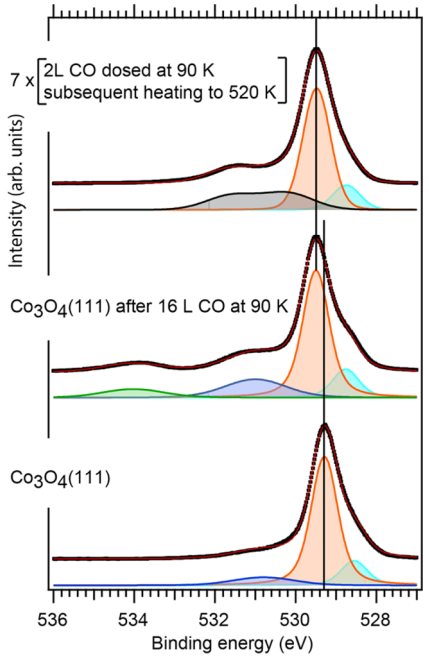

Figure 9. Comparison of O 1s spectra recorded on pristine Co_3O_4(111) (bottom), after adsorption adsorption of 16 L CO (middle), and after 7 adsorption (2 L CO)/desorption cycles to 520 K (top).

Figure 9 we compare the spectra recorded on the pristine film, after CO adsorption and after repeated adsorption/desorption cycles to 520 K. As discussed in section 3.3, the spectrum of the pristine film is dominated by an intense single feature at a BE of 529.3 eV (Figure 9, bottom spectra). Upon CO adsorption the

DOI: 10.1021/acs.jpcc.5b04145
J. Phys. Chem. C 2015, 119, 16688−16699

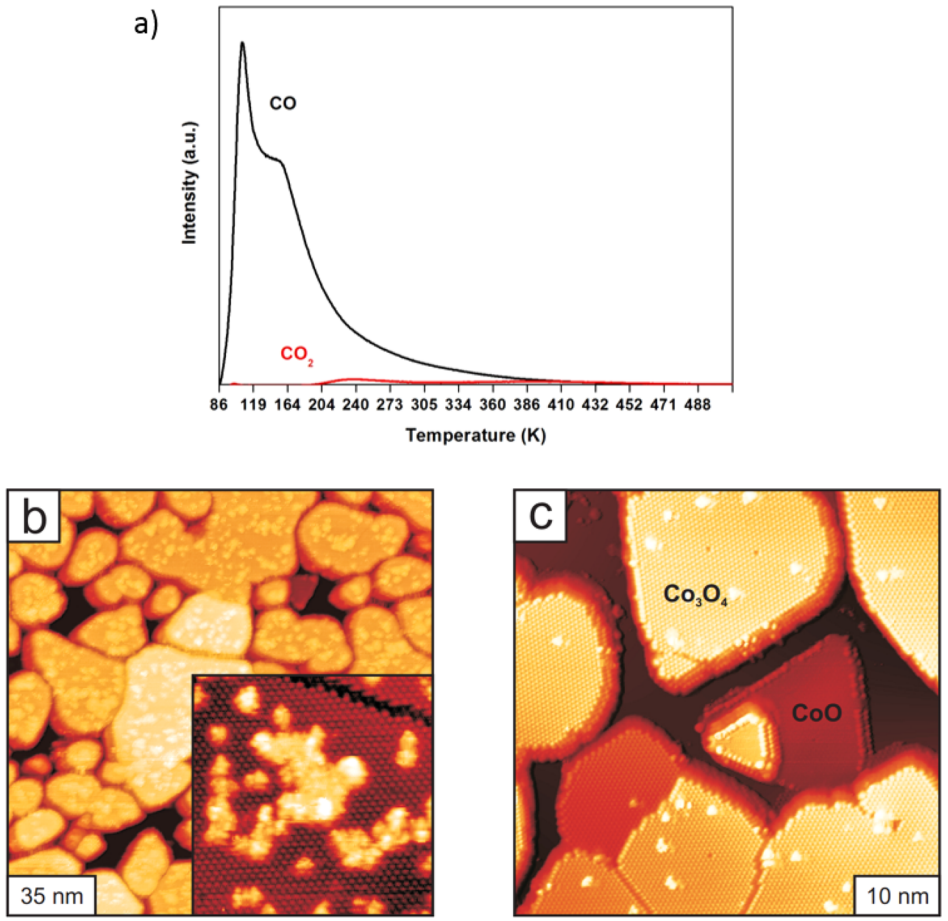

Figure 10. (a) TPD spectrum comparing the CO desorption (m/e = 28) and CO_2 production (m/e = 44) from a fully CO-saturated Co_3O_4(111) film; (b) STM image after four cycles of repeated CO adsorption and desorption up to a maximum temperature of 640 K; insert: close-up of the surface aggregates with perfect surrounding atomic lattice. (c) after annealing the film prepared in (b) to 740 K.

main component shifts by +0.2 eV and the two characteristic O 1s features shifted by +1.5 eV and +4.5 eV appear as discussed in section 3.3. After 7 cycles of CO adsorption and subsequent heating to 520 K, the main component also shifts by +0.2 eV, but now a new broad shoulder appears at the high binding energy side of the main peak. Curve fitting reveals that it is impossible to fit this shoulder component with one single component and we therefore used two components shifted by +0.7 eV (BE 530.0 eV) and +2.1 eV (BE 531.4 eV) for the curve fitting of this component. Further we note that the C 1s spectrum after repeated CO adsorption/desorption cycles (see Supporting Information) only reveals a very small carbonate component consistent with Figure 4c that showed that the large majority of carbonate disappeared at 520 K. Since we do not observe any significant amount of carbonate or any other carbon containing species on the Co_3O_4(111) surface after the repeated CO adsorption/desorption, it is evident that the broad O 1s shoulder at +0.7 to +2.1 eV must originate from the Co oxide film itself. A BE shoulder in this region has previously been assigned to oxygen vacancies in reducible oxides (see ref 59 and references therein). Further, the +0.2 eV shift of the O 1s main peak has been observed for reducible oxide films and again reflect a change of the electrostatic potential at the surface (see, e.g., refs 60−62). The assignment of the O 1s shoulder at +0.7 to +2.1 eV to oxygen vacancies can furthermore partly explain why the temperature development of the shoulder component in O 1s TPXPS experiments (Figure 6c) looks so complex, since this component is assigned to both carbonate and oxygen vacancies. We conclude that the process of CO_2 formation via carbonate decomposition involves the consumption of a small amount of lattice oxygen upon annealing.

This structural reorganization of the crystal in response to the loss of oxygen or equivalently the surplus of cobalt can be monitored by STM at the microscopic scale. After repeated cycles of CO adsorption and heating to 640 K we observe changes represented by the STM topography in Figure 10b. Whereas the overall morphology of the Co_3O_4 film does not change, we observe a high density of protrusions or flat clusters on the terraces (Figure 10b). Similar structures appear in the STM images also when evaporating small amounts of metallic Co onto the Co_3O_4 films. Therefore, we tentatively assign the clusters to cobalt-rich oxide aggregates at or right below the surface, which are formed as a reaction to the loss of lattice oxygen. We observe that the aggregates dissolve again in the Co_3O_4 crystallites if the oxide films are annealed to an even higher temperature of 740 K (Figure 10c). Eventually, the excess of Co (or loss of O) causes the complete crystallite to switch to rocksalt CoO(111), as observed especially for small crystallites (see Figure 10c). CoO(111) crystallites are readily identified by STM and also as faint diffraction spots in LEED.[35] According to the above discussion and by observing an essentially unchanged film morphology in STM, CO_2 formation and reduction of the Co_3O_4 films occurs exclusively via

DOI: 10.1021/acs.jpcc.5b04145
J. Phys. Chem. C 2015, 119, 16688−16699

formation of surface carbonates that are bound to defects such as step edges or side facets.

4. CONCLUSIONS

We have studied the interaction of CO and O_2 with well-ordered $Co_3O_4(111)$ films grown on Ir(100) using STM, TDS, HR-XPS, and IRAS under UHV conditions. The findings can be summarized as follows:

1. CO adsorbs on $Co_3O_4(111)$ at 100 K in two coverage regimes. At exposures below 1 L, a low coverage phase is formed in which the CO adsorbs on the topmost layer of Co^{2+} ions. This phase is characterized by a CO stretching mode with a singleton frequency at 2174 cm^{-1} (θ < 0.01). With increasing coverage the CO stretching band undergoes a redshift ($\Delta = -20$ cm^{-1}) to 2154 cm^{-1} at full coverage of the surface Co^{2+} ions (3.5×10^{14} molecules·cm^{-2}). At larger exposures, a compressed high coverage phase is formed, in which the CO is weakly adsorbed in between the Co^{2+} sites.
2. The weakly adsorbed molecular CO exhibits a complex C 1s spectrum which is associated with a strong charge transfer satellite structure. The C 1s main peak of this molecular CO is found at binding energy of 287.0 eV. Desorption of the molecularly adsorbed CO species gives rise to two desorption features in TDS at temperatures between 90 and 110 K and between 140 and 180 K, respectively. Repeated CO adsorption and desorption experiments show that the molecular CO species are adsorbed and desorbed reversibly.
3. In addition to the molecularly adsorbed CO, a bridging carbonate species is formed once the CO exposure exceeds a value of 1 L. This surface carbonate species is a minority species and forms at defects of the film most likely at steps and defect sites at the side facets of the (111) oriented grains. In contrast to the molecularly adsorbed CO, the surface carbonate species remains on the surface up to higher temperature. It desorbs in a broad temperature range between 200 and 400 K, indicating stronger binding and a substantial activation barrier for formation and desorption. Its IRAS signature is found at 1743−1751 cm^{-1} and the C 1s binding energy at 288.5 eV.
4. O_2 coadsorption does neither influence CO adsorption in the low coverage CO phase nor formation of the surface carbonate species. However, preadsorbed O_2 blocks the formation of the compressed high coverage CO phase.
5. Upon annealing, the surface carbonate decomposes mainly under formation of CO and to a very small extent under formation of CO_2. The latter process consumes lattice oxygen. The loss of oxygen is compensated by producing Co interstitials that segregate and form partially reduced oxide clusters at the surface. If a crystallite has lost too much lattice oxygen, it recrystallizes as a CoO grain.

ASSOCIATED CONTENT

Supporting Information

C 1s spectrum after repeated cycles of dosing CO and heating on $Co_3O_4(111)$/Ir(100). The Supporting Information is available free of charge on the ACS Publications website at DOI: 10.1021/acs.jpcc.5b04145.

AUTHOR INFORMATION

Corresponding Authors

*E-mail: alexander.schneider@fau.de. Phone: +49 9131 8528405. Fax: +49 9131 8528400.

*E-mail: joerg.libuda@fau.de. Phone: +49 9131 8527308. Fax: +49 9131 8528867.

Notes

The authors declare no competing financial interest.

ACKNOWLEDGMENTS

The authors gratefully acknowledge financial support by the Deutsche Forschungsgemeinschaft (DFG) within the DACH Project "COMCAT" and the DFG Research Unit 1878 "funCOS". The work was additionally supported within the Excellence Cluster "Engineering of Advanced Materials" in the framework of the Excellence Initiative and the Clariant AG. Further financial support by the European Commission ("chipCAT", FP7-NMP-2012-SMALL-6, Grant Agreement No. 310191), by COST Action CM1104 "Reducible oxide chemistry, structure and functions", and travel support by the DAAD is gratefully acknowledged. This work was also supported by the Röntgen-Ångström cluster "Catalysis on the atomic scale" (Project No. 349-2011-6491) and by the Project Grant 2012-3850 both financed by the Swedish research council. The MAX IV Laboratory personnel are acknowledged for support during measurements. The authors are grateful for the support of the Alexander von Humboldt Foundation within the Research Group Linkage Program.

REFERENCES

(1) Xie, X.; Li, Y.; Liu, Z.-Q.; Haruta, M.; Shen, W. Low-Temperature Oxidation of CO Catalysed by Co_3O_4 Nanorods. *Nature* **2009**, *458*, 746−749.

(2) Choudhary, T. V.; Banerjee, S.; Choudhary, V. R. Catalysts for Combustion of Methane and Lower Alkanes. *Appl. Catal., A* **2002**, *234*, 1−23.

(3) Jansson, J.; Palmqvist, A. E. C.; Fridell, E.; Skoglundh, M.; Osterlund, L.; Thormahlen, P.; Langer, V. On the Catalytic Activity of Co_3O_4 in Low-Temperature CO Oxidation. *J. Catal.* **2002**, *211*, 387−397.

(4) Liotta, L. F.; Wu, H.; Pantaleo, G.; Venezia, A. M. Co_3O_4 Nanocrystals and Co_3O_4-MO_x Binary Oxides for CO, CH_4 and VOC Oxidation at Low Temperatures: A Review. *Catal. Sci. Technol.* **2013**, *3*, 3085−3102.

(5) Xiong, S.; Yuan, C.; Zhang, M.; Xi, B.; Qian, Y. Controllable Synthesis of Mesoporous Co_3O_4 Nanostructures with Tunable Morphology for Application in Supercapacitors. *Chem. - Eur. J.* **2009**, *15*, 5320−5326.

(6) Zhao, Z.; Lin, X.; Jin, R.; Dai, Y.; Wang, G. High Catalytic Activity in CO Prox Reaction of Low Cobalt-Oxide Loading Catalysts Supported on Nano-Particulate CeO_2-ZrO_2 Oxides. *Catal. Commun.* **2011**, *12*, 1448−1451.

(7) Tuti, S.; Pepe, F. On the Catalytic Activity of Cobalt Oxide for the Steam Reforming of Ethanol. *Catal. Lett.* **2008**, *122*, 196−203.

(8) Wang, C.-B.; Lee, C.-C.; Bi, J.-L.; Siang, J.-Y.; Liu, J.-Y.; Yeh, C.-T. Study on the Steam Reforming of Ethanol over Cobalt Oxides. *Catal. Today* **2009**, *146*, 76−81.

(9) Dau, H.; Limberg, C.; Reier, T.; Risch, M.; Roggan, S.; Strasser, P. The Mechanism of Water Oxidation: From Electrolysis Via Homogeneous to Biological Catalysis. *ChemCatChem* **2010**, *2*, 724−761.

(10) Liang, Y.; Li, Y.; Wang, H.; Zhou, J.; Wang, J.; Regier, T.; Dai, H. Co_3O_4 Nanocrystals on Graphene as a Synergistic Catalyst for Oxygen Reduction Reaction. *Nat. Mater.* **2011**, *10*, 780−786.

DOI: 10.1021/acs.jpcc.5b04145
J. Phys. Chem. C 2015, 119, 16688−16699

(11) Xu, C.; Tian, Z.; Shen, P.; Jiang, S. P. Oxide (CeO_2, NiO, Co_3O_4 and Mn_3O_4-Promoted Pd/C Electrocatalysts for Alcohol Electrooxidation in Alkaline Media. *Electrochim. Acta* **2008**, *53*, 2610−2618.
(12) Vargas, J. C.; Libs, S.; Roger, A. C.; Kiennemann, A. Study of Ce-Zr-Co Fluorite-Type Oxide as Catalysts for Hydrogen Production by Steam Reforming of Bioethanol. *Catal. Today* **2005**, *107*−*08*, 417−425.
(13) Yao, Y. Y. Oxidation of Hydrocarbons and CO over Metal-Oxides 0.3. Co_3O_4. *J. Catal.* **1974**, *33*, 108−122.
(14) Jansson, J. Low-Temperature CO Oxidation over Co_3O_4/Al_2O_3. *J. Catal.* **2000**, *194*, 55−60.
(15) Thormahlen, P.; Skoglundh, M.; Fridell, E.; Andersson, B. Low-Temperature CO Oxidation over Platinum and Cobalt Oxide Catalysts. *J. Catal.* **1999**, *188*, 300−310.
(16) Royer, S.; Duprez, D. Catalytic Oxidation of Carbon Monoxide over Transition Metal Oxides. *ChemCatChem* **2011**, *3*, 24−65.
(17) Yu, Y.; Takei, T.; Ohashi, H.; He, H.; Zhang, X.; Haruta, M. Pretreatments of Co_3O_4 at Moderate Temperature for CO Oxidation at −80 °C. *J. Catal.* **2009**, *267*, 121−128.
(18) Tang, C.-W.; Hsu, L.-C.; Yu, S.-W.; Wang, C.-B.; Chien, S.-H. In Situ FT-IR and TPD-MS Study of Carbon Monoxide Oxidation over a CeO_2/Co_3O_4 Catalyst. *Vib. Spectrosc.* **2013**, *65*, 110−115.
(19) Hu, L.; Sun, K.; Peng, Q.; Xu, B.; Li, Y. Surface Active Sites on Co_3O_4 Nanobelt and Nanocube Model Catalysts for CO Oxidation. *Nano Res.* **2010**, *3*, 363−368.
(20) Pollard, M. J.; Weinstock, B. A.; Bitterwolf, T. E.; Griffiths, P. R.; Newbery, A. P.; Paine, J. B., III. A Mechanistic Study of the Low-Temperature Conversion of Carbon Monoxide to Carbon Dioxide over a Cobalt Oxide Catalyst. *J. Catal.* **2008**, *254*, 218−225.
(21) Ma, C.; Wang, D.; Xue, W.; Dou, B.; Wang, H.; Hao, Z. Investigation of Formaldehyde Oxidation over Co_3O_4-CeO_2 and Au/Co_3O_4-CeO_2 Catalysts at Room Temperature: Effective Removal and Determination of Reaction Mechanism. *Environ. Sci. Technol.* **2011**, *45*, 3628−3634.
(22) Ma, C. Y.; Mu, Z.; Li, J. J.; Jin, Y. G.; Cheng, J.; Lu, G. Q.; Hao, Z. P.; Qiao, S. Z. Mesoporous Co_3O_4 and Au/Co_3O_4 Catalysts for Low-Temperature Oxidation of Trace Ethylene. *J. Am. Chem. Soc.* **2010**, *132*, 2608−2613.
(23) Cunningham, D. A. H.; Kobayashi, T.; Kamijo, N.; Haruta, M. Influence of Dry Operating-Conditions - Observation of Oscillations and Low-Temperature CO Oxidation over Co_3O_4 and Au/Co_3O_4 Catalysts. *Catal. Lett.* **1994**, *25*, 257−264.
(24) Luo, J.-Y.; Meng, M.; Li, X.; Li, X.-G.; Zha, Y.-Q.; Hu, T.-D.; Xie, Y.-N.; Zhang, J. Mesoporous Co_3O_4-CeO_4 and Pd/Co_3O_4-CeO_2 Catalysts: Synthesis, Characterization and Mechanistic Study of Their Catalytic Properties for Low-Temperature CO Oxidation. *J. Catal.* **2008**, *254*, 310−324.
(25) Finocchio, E.; Busca, G.; Lerenzelli, V.; Escribano, V. S. FTIR Studies on the Selective Oxidation and Combustion of Light Hydrocarbons at Metal Oxide Surfaces Part 2. Propane and Propene Oxidation on Co_3O_4. *J. Chem. Soc., Faraday Trans.* **1996**, *92*, 1587−1593.
(26) Finocchio, E.; Willey, R. J.; Busca, G.; Lorenzelli, V. FTIR Studies on the Selective Oxidation and Combustion of Light Hydrocarbons at Metal Oxide Surfaces Part 3. Comparison of the Oxidation of C-3 Organic Compounds over Co_3O_4, $MgCr_2O_4$ and CuO. *J. Chem. Soc., Faraday Trans.* **1997**, *93*, 175−180.
(27) Busca, G.; Daturi, M.; Finocchio, E.; Lorenzelli, V.; Ramis, G.; Willey, R. J. Transition Metal Mixed Oxides as Combustion Catalysts: Preparation, Characterization and Activity Mechanisms. *Catal. Today* **1997**, *33*, 239−249.
(28) Liang, Y.; et al. Oxygen Reduction Electrocatalyst Based on Strongly Coupled Cobalt Oxide Nanocrystals and Carbon Nanotubes. *J. Am. Chem. Soc.* **2012**, *134*, 15849−15857.
(29) Jiang, D.-e.; Dai, S. The Role of Low-Coordinate Oxygen on Co_3O_4(110) in Catalytic CO Oxidation. *Phys. Chem. Chem. Phys.* **2011**, *13*, 978−984.
(30) Hu, L.; Peng, Q.; Li, Y. Selective Synthesis of Co_3O_4 Nanocrystal with Different Shape and Crystal Plane Effect on Catalytic Property for Methane Combustion. *J. Am. Chem. Soc.* **2008**, *130*, 16136−16137.
(31) Fei, Z.; He, S.; Li, L.; Ji, W.; Au, C.-T. Morphology-Directed Synthesis of Co_3O_4 Nanotubes Based on Modified Kirkendall Effect and Its Application in CH_4 Combustion. *Chem. Commun.* **2012**, *48*, 853−855.
(32) Kuhlenbeck, H.; Shaikhutdinov, S.; Freund, H.-J. Well-Ordered Transition Metal Oxide Layers in Model Catalysis - a Series of Case Studies. *Chem. Rev.* **2013**, *113*, 3986−4034.
(33) Libuda, J.; Freund, H. J. Molecular Beam Experiments on Model Catalysts. *Surf. Sci. Rep.* **2005**, *57*, 157−298.
(34) Meyer, W.; Biedermann, K.; Gubo, M.; Hammer, L.; Heinz, K. Surface Structure of Polar Co_3O_4(111) Films Grown Epitaxially on Ir(100)-(1 × 1). *J. Phys.: Condens. Matter* **2008**, *20*, 265011.
(35) Biedermann, K.; Gubo, M.; Hammer, L.; Heinz, K. Phases and Phase Transitions of Hexagonal Cobalt Oxide Films on Ir(100)-(1 × 1). *J. Phys.: Condens. Matter* **2009**, *21*, 185003.
(36) Gubo, M.; Ebensperger, C.; Meyer, W.; Hammer, L.; Heinz, K. Structural Elements in the Oxidation Process of a Single Cobalt Layer on Ir(100)-(1 × 1). *Phys. Rev. B* **2011**, *83*, 075435.
(37) Gubo, M.; Ebensperger, C.; Meyer, W.; Hammer, L.; Heinz, K.; Mittendorfer, F.; Redinger, J. Tuning the Growth Orientation of Epitaxial Films by Interface Chemistry. *Phys. Rev. Lett.* **2012**, *108*, 066101.
(38) Heinz, K.; Hammer, L. Epitaxial Cobalt Oxide Films on Ir(100)-the Importance of Crystallographic Analyses. *J. Phys.: Condens. Matter* **2013**, *25*, 173001.
(39) Feulner, P.; Menzel, D. Simple Ways to Improve Flash Desorption Measurements from Single-Crystal Surfaces. *J. Vac. Sci. Technol.* **1980**, *17*, 662−663.
(40) Ghosh, P.; Narasimhan, S.; Jenkins, S. J.; King, D. A. Lifting of Ir{100} Reconstruction by CO Adsorption: An Ab Initio Study. *J. Chem. Phys.* **2007**, *126*, 244701.
(41) Nyholm, R.; Andersen, J. N.; Johansson, U.; Jensen, B. N.; Lindau, I. Beamline I311 at Max-Lab: A Vuv/Soft X-ray Undulator Beamline for High Resolution Electron Spectroscopy. *Nucl. Instrum. Methods Phys. Res., Sect. A* **2001**, *467*, 520−524.
(42) Heidberg, J.; Kandel, M.; Meine, D.; Wildt, U. The Monolayer CO Adsorbed on MgO(100) Detected by Polarization Infrared-Spectroscopy. *Surf. Sci.* **1995**, *331*, 1467−1472.
(43) Spoto, G.; Gribov, E. N.; Ricchiardi, G.; Damin, A.; Scarano, D.; Bordiga, S.; Lamberti, C.; Zecchina, A. Carbon Monoxide MgO from Dispersed Solids to Single Crystals: A Review and New Advances. *Prog. Surf. Sci.* **2004**, *76*, 71−146.
(44) Spoto, G.; Gribov, E.; Damin, A.; Ricchiardi, G.; Zecchina, A. The IR Spectra of Mg-$5c^{2+}$(CO) Complexes on the (001) Surfaces of Polycrystalline and Single Crystal MgO. *Surf. Sci.* **2003**, *540*, L605−L610.
(45) Zecchina, A.; Scarano, D.; Bordiga, S.; Ricchiardi, G.; Spoto, G.; Geobaldo, F. IR Studies of CO and NO Adsorbed on Well Characterized Oxide Single Microcrystals. *Catal. Today* **1996**, *27*, 403−435.
(46) Lemire, C.; Meyer, R.; Henrich, V. E.; Shaikhutdinov, S.; Freund, H. J. The Surface Structure of Fe_3O_4(111) Films as Studied by CO Adsorption. *Surf. Sci.* **2004**, *572*, 103−114.
(47) Solymosi, F.; Knozinger, H. Infrared Study on the Interaction of CO with Alumina-Supported Rhodium. *J. Chem. Soc., Faraday Trans.* **1990**, *86*, 389−395.
(48) Frank, M.; Kuhnemuth, R.; Baumer, M.; Freund, H. J. Vibrational Spectroscopy of CO Adsorbed on Supported Ultra-Small Transition Metal Particles and Single Metal Atoms. *Surf. Sci.* **2000**, *454*, 968−973.
(49) Vayssilov, G. N.; Mihaylov, M.; St. Petkov, P.; Hadjiivanov, K. I.; Neyman, K. M. Reassignment of the Vibrational Spectra of Carbonates, Formates, and Related Surface Species on Ceria: A Combined Density Functional and Infrared Spectroscopy Investigation. *J. Phys. Chem. C* **2011**, *115*, 23435−23454.

DOI: 10.1021/acs.jpcc.5b04145
J. Phys. Chem. C 2015, 119, 16688−16699

(50) Yanagisawa, Y.; Takaoka, K.; Yamabe, S.; Ito, T. Interaction of CO_2 with Magnesium-Oxide Surfaces - a TPD, FTIR, and Cluster-Model Calculation Study. *J. Phys. Chem.* **1995**, *99*, 3704−3710.
(51) Neitzel, A.; Lykhach, Y.; Skala, T.; Tsud, N.; Vorokhta, M.; Mazur, D.; Prince, K. C.; Matolin, V.; Libuda, J. Surface Sites on Pt-CeO_2 Mixed Oxide Catalysts Probed by CO Adsorption: A Synchrotron Radiation Photoelectron Spectroscopy Study. *Phys. Chem. Chem. Phys.* **2014**, *16*, 24747−24754.
(52) Fuggle, J. C.; Umbach, E.; Menzel, D.; Wandelt, K.; Brundle, C. R. Adsorbate Line-Shapes and Multiple Lines in XPS - Comparison of Theory and Experiment. *Solid State Commun.* **1978**, *27*, 65−69.
(53) Tillborg, H.; Nilsson, A.; Martensson, N. Shake-up and Shake-Off Structures in Core-Level Photoemission Spectra from Adsorbates. *J. Electron Spectrosc. Relat. Phenom.* **1993**, *62*, 73−93.
(54) Cappus, D.; et al. Electronic and Geometric Structure of Adsorbates on Oxide Surfaces. *J. Electron Spectrosc. Relat. Phenom.* **1994**, *68*, 347−355.
(55) Sandell, A.; Bennich, P.; Nilsson, A.; Hernnas, B.; Bjorneholm, O.; Martensson, N. Chemisorption of CO on Cu(100), Ag(110) and Au(110). *Surf. Sci.* **1994**, *310*, 16−26.
(56) Haeming, M.; Schoell, A.; Umbach, E.; Reinert, F. Adsorbate-Substrate Charge Transfer and Electron-Hole Correlation at Adsorbate/Metal Interfaces. *Phys. Rev. B* **2012**, *85*, 235132.
(57) Knudsen, J.; Martin, N. M.; Grånäs, E.; Blomberg, S.; Gustafson, J.; Andersen, J. N.; Lundgren, E.; Klacar, S.; Hellman, A.; Gronbeck, H. Carbonate Formation on p(4 × 4)-O/Ag(111). *Phys. Rev. B* **2011**, *84*, 115430.
(58) Andersson, S.; et al. Metal-Oxide Interaction for Metal Clusters on a Metal-Supported Thin Alumina Film. *Surf. Sci.* **1999**, *442*, L964−L970.
(59) Lykhach, Y.; et al. Water Chemistry on Model Ceria and Pt/Ceria Catalysts. *J. Phys. Chem. C* **2012**, *116*, 12103−12113.
(60) Lykhach, Y.; Happel, M.; Johanek, V.; Skala, T.; Kollhoff, F.; Tsud, N.; Dvorak, F.; Prince, K. C.; Matolin, V.; Libuda, J. Adsorption and Decomposition of Formic Acid on Model Ceria and Pt/Ceria Catalysts. *J. Phys. Chem. C* **2013**, *117*, 12483−12494.
(61) Chen, T. L.; Mullins, D. R. Adsorption and Reaction of Acetaldehyde over CeO_x(111) Thin Films. *J. Phys. Chem. C* **2011**, *115*, 3385−3392.
(62) Mullins, D. R.; Robbins, M. D.; Zhou, J. Adsorption and Reaction of Methanol on Thin-Film Cerium Oxide. *Surf. Sci.* **2006**, *600*, 1547−1558.

DOI: 10.1021/acs.jpcc.5b04145
J. Phys. Chem. C 2015, 119, 16688−16699